

Dynamic Magnetic Resonance Inverse Imaging of Human Brain Function

Fa-Hsuan Lin,^{1,2*} Lawrence L. Wald,^{1,2} Seppo P. Ahlfors,^{1,2} Matti S. Hämäläinen,^{1,2} Kenneth K. Kwong,^{1,2} and John W. Belliveau^{1,2}

MRI is widely used for noninvasive hemodynamic-based functional brain imaging. In traditional spatial encoding, however, gradient switching limits the temporal resolution, which makes it difficult to unambiguously identify possible fast nonhemodynamic changes. In this paper we propose a novel reconstruction approach, called dynamic inverse imaging (InI), that is capable of providing millisecond temporal resolution when highly parallel detection is used. To achieve an order-of-magnitude speedup in generating time-resolved contrast estimates and dynamic statistical parametric maps (dSPMs), the spatial information is derived from an array of detectors rather than by time-consuming gradient-encoding methods. The InI approach was inspired by electroencephalography (EEG) and magnetoencephalography (MEG) source localization techniques. Dynamic MR InI was evaluated by means of numerical simulations. InI was also applied to measure BOLD hemodynamic time curves at 20-ms temporal resolution in a visual stimulation experiment using a 90-channel head array. InI is expected to improve the time resolution of MRI and provide increased flexibility in the trade-off between spatial and temporal resolution for studies of dynamic activation patterns in the human brain. Magn Reson Med 56:787–802, 2006. © 2006 Wiley-Liss, Inc.

Key words: MRI; inverse; parallel MRI; magnetoencephalography; minimum-norm; MNE; dSPM; InI; electroencephalography

Single-shot fast MRI with 1–3-s time resolution has been the principal technology for functional MRI (fMRI) (1–4). This time resolution is adequate for observing hemodynamic responses (HDRs), which are secondary to the much faster neural activity (5). Because of its high spatial resolution, noninvasiveness, and flexibility of contrast preparation, MRI has also been considered for its potential to further detect fast, nonhemodynamic functional changes related to human brain activity (6,7). However, efforts to identify suitable MRI contrast mechanisms have been hampered by the lack of required temporal resolution. Ultrafast MRI (100 frames per second or more) is a mandatory tool for testing any novel direct neuronal contrast mechanisms. It may not be possible to discern a contrast change that occurs and then disappears on a 10-ms scale

without an imaging technique with similar temporal resolution. Thus, a fast imaging technique with millisecond temporal resolution is indispensable as the prerequisite for allowing MR to probe direct neural contrast mechanisms.

In traditional Fourier MRI, the temporal resolution is constrained by the *k*-space traversing scheme used to spatially encode the data. Echo-planar imaging (EPI) (8) and spiral imaging (9) utilize switching gradients to achieve *k*-space traversing at a faster imaging rate than gradient-echo or spin-echo imaging. With state-of-the-art technology, 2D single-slice T_2^* -weighted images can be obtained in approximately 80 ms by EPI or spiral imaging. This allows whole-head coverage with 3-mm isotropic resolution in 2–3 s. Modest improvements can be made by optimizing the *k*-space sampling and reconstruction methods. For example, instead of completing the *k*-space traversal for every measurement, accelerated MR data acquisition can be achieved by various alterations of the *k*-space trajectories and the associated image reconstruction algorithms, such as partial *k*-space sampling (10). Alternatively, a priori information-based methods can also improve the temporal resolution of MR dynamic measurements (11) with various implementations, such as keyhole imaging (12), singular value decomposition (SVD) MRI (13), and wavelet-encoded MRI (14). Rather than a direct measurement, it has been demonstrated that manipulating experimental design can obtain fMRI with millisecond temporal resolution (15).

Parallel MRI methods using spatial information derived from the spatial distribution of the coils in the array have been proposed to accelerate MRI scanning. These include the *k*-space simultaneous acquisition of spatial harmonics (SMASH) (16), generalized autocalibrating partially parallel acquisitions (GRAPPA) (17), and image domain sensitivity encoding (SENSE) (18) methods, all of which share a similar theoretical background (19). Parallel MRI accelerates image data acquisition at the cost of a reduced signal-to-noise ratio (SNR). The temporal acceleration rate is limited by the number of coils in the array and by the phase-encoding schemes used, and typically acceleration factors of 2 or 3 are achieved. Incorporating a static image as prior information has been shown to further improve the sensitivity of fMRI using a parallel MRI technique (20).

The attainable acceleration in parallel MRI is limited by the available independent spatial information among the channels in the array. Mathematically, the parallel MRI image reconstruction requires solving an overdetermined linear system using this spatial information. Advances in the coil array design with more channels can increase the acceleration rate in parallel MRI. Recently, optimized head coil arrays have been extended from eight-channel (21) to 16-channel (22) and 23-, 32-, and 90-channel (23,24) ar-

¹Athinoula A. Martinos Center for Biomedical Imaging, Massachusetts General Hospital, Charlestown, Massachusetts, USA.

²Department of Radiology, Massachusetts General Hospital, Charlestown, Massachusetts, USA.

Grant sponsor: National Institutes of Health; Grant numbers: R01 HD040712; R01 NS037462; R01 EB00079004; P41 RR14075; Grant sponsor: Mental Illness and Neuroscience Discovery Institute (MIND).

*Correspondence to: Fa-Hsuan Lin, Ph.D., Athinoula A. Martinos Center for Biomedical Imaging, Bldg. 149, 13th Street, Mailcode 149-2301, Charlestown, MA 02129. E-mail: fhlin@nmr.mgh.harvard.edu

Received 7 November 2005; revised 19 May 2006; accepted 23 May 2006.

DOI 10.1002/mrm.20997

Published online 8 September 2006 in Wiley InterScience (www.interscience.wiley.com).

rays. Interestingly, the geometric configuration of our 90-channel head array is similar to that of the electrodes or superconductive quantum interference device (SQUID) sensors in modern EEG and MEG systems (25). The MEG sensors detect magnetic fields generated by neural currents (25), while MRI detects oscillating electromagnetic fields from magnetization precession (26). Whereas MEG derives all of its spatial information from the geometry of the detector array, accelerated MRI still relies heavily on gradient encoding.

Recently, a dedicated 64-channel linear planar array was developed to achieve 64-fold acceleration using single-echo acquisition (SEA) and SENSE reconstruction (27). The SEA approach depends on the linear array layout and localized RF coil sensitivity in individual channels to eliminate the phase-encoding steps required in conventional imaging. The challenge of this approach is the limited sensitivity in the perpendicular direction to the array plane, and the extension of the methodology to head-shaped geometries. In the present work we addressed these issues by developing an MR reconstruction method that was inspired by MEG source localization and utilizes a similar detector array layout. We attempted to minimize the gradient encoding and to reconstruct brain images using only a single point or single line of k -space.

The goal of this work was to perform functional brain imaging using MRI with high temporal resolution. We sought estimates of dynamic spatially resolved changes and statistical parametric maps (SPMs) for both hemodynamic response (HDR) and potential changes directly related to neural activity. The proposed MR inverse imaging (InI) method represents a transition from the overdetermined linear system in traditional parallel MRI reconstruction to an underdetermined one. The novelty of this approach is that it combines a large- N coil array with a linear estimation approach to achieve an order-of-magnitude speedup in the acquisition of dynamic brain MRI (20 ms temporal resolution). Since both novel contrast mechanisms and ultrafast imaging are needed to ultimately image “direct” neuronal responses on the millisecond scale, ultrafast encoding is an enabling technology, without which it is difficult to even unambiguously test a contrast mechanism. Indeed, today’s “rapid” imaging (EPI in particular) was the enabling technology that led to the first hemodynamic-based fMRI studies in the early 1990s (1–4). In the following, we introduce a theoretical framework, experimental procedures, and results from simulations and in vivo HDR measurements to evaluate the proposed InI methodology.

THEORY

Here we describe a theoretical framework for MR InI and its application to dynamic measurements to generate time-resolved dynamic SPMs (dSPMs) of brain activation. The framework includes 1D, 2D, and 3D InI. Specifically, the spatial information derived from an array of RF coils enables estimates of the dynamic changes and associated dSPMs to be obtained. We attempt to combine the concepts, definitions, and notation of both conventional parallel MR reconstruction (18) and MEG source localization reconstruction (25) into a single framework.

Forward Problem

The generation of time-series images $\mathbf{y}(t)$ on an n_c -channel RF coil array in MRI can be formulated as:

$$\mathbf{y}(t) = \mathbf{A}\mathbf{x}(t) + \mathbf{n}(t), \quad [1]$$

where t indicates time, and $\mathbf{y}(t)$ is an $(n_a \cdot n_c)$ -by-1 vector with n_a vertical stacks (of k -space samples) with n_c observations (number of array channels), $\mathbf{x}(t)$ is an n_p -by-1 image vector to be reconstructed, $\mathbf{n}(t)$ is a $(n_a \cdot n_c)$ -by-1 vector denoting the contaminating noise, and the matrix \mathbf{A} is the “forward operator,” which maps the signals to the coil array observations. Here we introduce the symbol r to indicate the “acceleration rate,” the ratio between the number of fully sampled k -space data (n_p) and the number of k -space samples in the accelerated dynamic scan (n_a). In traditional parallel MRI, $n_a \leq n_p$. In Fourier MRI, the forward operator for n^{th} coil in the array can be further decomposed into Fourier encoding part (\mathbf{E}) and coil sensitivity modulation part (\mathbf{P}_n):

$$\mathbf{A}_n = \mathbf{E}\mathbf{P}_n, \quad n = 1 \cdot \cdot \cdot n_c, \quad \mathbf{A} = \begin{bmatrix} \mathbf{A}_1 \\ \vdots \\ \mathbf{A}_{n_c} \end{bmatrix}. \quad [2]$$

The coil sensitivity describes how the spin density is modulated by the reception profile of each channel in the RF array and thus differs among the coil array elements. The Fourier encoding matrix, however, is identical for all coils in the array due to the same applied gradients. Given the k -space trajectory, $\mathbf{E} = \Phi_{n_a}^{-1} \mathbf{S} \Phi_{n_p}$, where \mathbf{S} is the sampling matrix of size n_a -by- n_p consisting of row vectors of the discrete delta function. In the i^{th} row of \mathbf{S} , the j^{th} element is one if the k -space spatially indexed entry j is sampled, and zero otherwise. Φ_{n_p} is the discrete Fourier transform matrix of size n_p -by- n_p . In addition, we can also incorporate the off-resonance phase information and thus formulate the “phase-constrained” forward matrix (28):

$$\mathbf{A}_n = \mathbf{E}\mathbf{P}_n\Theta, \quad n = 1 \cdot \cdot \cdot n_c, \quad \mathbf{A} = \begin{bmatrix} \mathbf{A}_1 \\ \vdots \\ \mathbf{A}_{n_c} \end{bmatrix}, \quad [3]$$

where Θ is a diagonal matrix with diagonal entries describing the off-resonance phase shift. In cases without any off-resonance, Θ is an identity matrix. By factoring out the real and imaginary parts, we can constrain the reconstructed image $\mathbf{x}(t)$ to be real-valued:

$$\begin{bmatrix} \text{Re}\{\mathbf{y}(t)\} \\ \text{Im}\{\mathbf{y}(t)\} \end{bmatrix} = \begin{bmatrix} \text{Re}\{\mathbf{A}\} \\ \text{Im}\{\mathbf{A}\} \end{bmatrix} \mathbf{x}(t) + \begin{bmatrix} \text{Re}\{\mathbf{n}(t)\} \\ \text{Im}\{\mathbf{n}(t)\} \end{bmatrix}, \quad [4]$$

Phase constraint was previously proposed for parallel MRI reconstruction (28,29). The purpose of the phase-constrained forward problem is to enable dynamic statistical inference with either a positive or negative estimate of $\mathbf{x}(t)$ to infer the MR signal to be higher or lower than the baseline signal. This is because we explicitly constrain $\mathbf{x}(t)$ to be a real-valued vector. We describe the details in the “dynamic statistical parametric map (dSPM)” section below.

With the use of repeated parallel MRI acquisitions, noise can be characterized with a noise covariance matrix, \mathbf{C} . The forward problem is first whitened to facilitate the formulation without a loss of generality. Employing the Cholesky decomposition of the noise covariance matrix $\mathbf{C} = (\mathbf{C}^{1/2})^H(\mathbf{C}^{1/2})$, where $\mathbf{C}^{1/2}$ is an upper-triangular matrix, the whitened forward equation is:

$$\mathbf{y}_w(t) = \mathbf{A}_w \mathbf{x}(t) + \mathbf{n}_w(t), \quad [5]$$

where $\mathbf{y}_w(t) = \mathbf{C}^{-1/2} \mathbf{y}(t)$, $\mathbf{A}_w = \mathbf{C}^{-1/2} \mathbf{A}$, and $\langle \mathbf{n}_w(t) \mathbf{n}_w(t)^H \rangle = \mathbf{I}_{n_c}$. The superscript H indicates the complex conjugate and transpose, $\langle \bullet \rangle$ represents the average across ensembles, and \mathbf{I}_{n_c} is the identity matrix of size n_c -by- n_c .

Source Space

In MR InI, the spatial locations corresponding to the elements of $\mathbf{x}(t)$ constitute the source space. In practice, the source space can be a 3D volumetric space representing multiple partitions in conventional 3D MRI. This 3D InI source space corresponds to using nonselective excitation over the whole brain, and acquires only the central point of the k -space volume for InI reconstruction. It is also possible to have a 2D planar source space if a slice-selection gradient is employed to constrain the image to be reconstructed from a single plane (2D InI). Similarly, a 1D linear source space is possible if both slice-selection and frequency-encoding gradients are employed in Fourier imaging (1D InI). In the latter case, the only uncertainty in spatial localization is in the phase-encoding direction, and we will resort to coil sensitivity profile to resolve it. Incorporating a limited amount of phase-encoding steps, such as in traditional parallel MRI SENSE/SMASH/GRAPPA k -space sampling patterns, can further restrict the source space. Subsequent derivation of InI image reconstruction will show that traditional SENSE/SMASH/GRAPPA imaging is a special case of InI with an overdetermined linear system. The choice of the configuration of the source space will determine the temporal resolution of the dynamic InI. There is a trade-off between the time required for slice-selection, frequency-encoding, and phase-encoding gradient cycling.

Prior Information and Baseline Measurements

In dynamic imaging, prior information about the solution is usually available. We previously demonstrated that incorporating priors can improve the image reconstruction quality in anatomical and dynamic fMRI (20,30). Here we will also include the option of using priors in the dynamic InI framework. Denoting the time-invariant prior for the solution by \mathbf{x}_0 , the forward problem can be rewritten as

$$\mathbf{y}'_w(t) = \mathbf{A}_w \mathbf{x}'(t) + \mathbf{n}_w(t), \quad [6]$$

where $\mathbf{x}'(t) = \mathbf{x}(t) - \mathbf{x}_0$. The subsequent derivation of the minimum-norm solution will incorporate the prior information to yield time-resolved images $\mathbf{x}(t)$. However, if no prior information is available, we can experimentally define the “baseline interval” to estimate the $\mathbf{A}_w \mathbf{x}_0$ term. For example, analogously to MEG/EEG evoked response ex-

periments, the averaged InI accelerated measurements over baseline interval can generate the averaged baseline activity estimate, which will be subtracted from dynamic InI measurements in the “activity interval” to generate $\mathbf{y}'_w(t)$. In the following section, we show that the spatial distribution of the dynamic change can be still be resolved based simply on $\mathbf{y}'_w(t)$ without spatial prior \mathbf{x}_0 .

Minimum-Norm Estimate (MNE)

The stability of the solution for $\mathbf{x}'(t)$ depends on the condition of the forward matrix. Traditional parallel MRI limits the forward operator such that \mathbf{A}_w has more rows than columns. In practice, this constrains the acceleration rate (r) to be less than or equal to the number of the coils in the array (n_c). Mathematically, this is equivalent to the requirement of the existence of $(\mathbf{A}_w^H \mathbf{A}_w)^{-1}$. This is explicitly required in SENSE and GRAPPA image reconstructions. Nevertheless, in highly accelerated cases, the Fourier encoding matrix has very small number of rows, and thus $(\mathbf{A}_w^H \mathbf{A}_w)$ is very ill-conditioned. In other words, dynamic InI may encounter the inverse problem where there are more unknowns than observations. A unique solution to the ill-posed dynamic InI can be obtained by adding constraints. One common choice is the MNE:

$$\mathbf{x}'(t) = \arg \min_{\mathbf{x}'} \{ \|\mathbf{y}'_w(t) - \mathbf{A}_w \mathbf{x}'(t)\|_2^2 + \lambda^2 \|\mathbf{R}^{-1/2} \mathbf{x}'(t)\|_2^2 \}, \quad [7]$$

where $\|\bullet\|_2^2$ is the square of the ℓ_2 -norm, λ^2 is a regularization parameter, and \mathbf{R} is the source covariance matrix

$$\mathbf{R} = \langle \mathbf{x}'(t) \mathbf{x}'(t)^H \rangle = \langle \mathbf{x}(t) \mathbf{x}(t)^H \rangle. \quad [8]$$

The cost function in Eq. [7] consists of two parts: the first is the model error term, which quantifies the discrepancy between measured and modeled data, and the second is the prior error term, which quantifies the solution deviation from the prior. The second term in the cost function implies the distance away from the prior \mathbf{x}_0 (in the ℓ_2 -norm sense). The solution is provided by the linear inverse operator \mathbf{W}_w :

$$\hat{\mathbf{x}}'(t) = \mathbf{W}_w \mathbf{y}'_w(t) = \mathbf{R} \mathbf{A}_w^H (\mathbf{A}_w \mathbf{R} \mathbf{A}_w^H + \lambda^2 \mathbf{I}_N)^{-1} \mathbf{y}'_w(t). \quad [9]$$

The calculation of the source covariance matrix \mathbf{R} assumes that a dynamically changing image is superimposed on a static image. Note that in the calculation of \mathbf{R} , the stationary part of the image is removed. Thus, only pixels with dynamic changes contribute to the estimate of \mathbf{R} , whereas the static image does not affect the estimate of \mathbf{R} . Experimentally, \mathbf{R} can be estimated from repetitive measurements of the fully sampled k -space data with the assumption of no motion artifact during data acquisition. Theoretically, \mathbf{R} is given as a spatial prior in the Bayesian modeling framework, and it indicates the spatial distribution of the likelihood of contributing dynamic changes from different voxels. If no estimate for \mathbf{R} is available, \mathbf{R} may be specified as an identity matrix corresponding to an equal likelihood everywhere in the image contributing to the observed dynamic change. However, a better specifi-

cation of source covariance matrix \mathbf{R} may improve the localization accuracy of dynamic changes.

The specification of the regularization parameter results in a trade-off between the model error term and the prior error term. Practically, it can be chosen from automatic regularization techniques, such as L-curve (30,31). Here we used an algorithm to estimate λ^2 based on the whitened observation and SNR estimates (32).

Given the static prior image, the estimate of the image is

$$\begin{aligned}\hat{\mathbf{x}}(t) &= \hat{\mathbf{x}}'(t) + \mathbf{x}_0 = \mathbf{W}_w \mathbf{y}'_w(t) + \mathbf{x}_0 = \mathbf{W}_w \mathbf{y}_w(t) + (\mathbf{I} - \boldsymbol{\Psi}) \mathbf{x}_0 \\ &= \mathbf{W}_w \mathbf{y}_w(t) + \Delta \mathbf{x}_0, \quad [10]\end{aligned}$$

where $\boldsymbol{\Psi} = \mathbf{W}_w \mathbf{A}_w$ denotes the resolution kernel, and $\Delta = \mathbf{I} - \boldsymbol{\Psi}$ denotes the deviation kernel. The resolution kernel is important for quantifying the spatial resolution of the InI image reconstruction, as discussed in the following section.

Relationship Between Over- and Underdetermined Reconstructions

The MNE of the dynamic InI can be generalized to the traditional parallel MRI as the case of underdetermined parallel MRI reconstruction. Assuming that $(\mathbf{A}_w \mathbf{R} \mathbf{A}_w^H + \lambda^2 \mathbf{I}_N)$ and $(\mathbf{A}_w^H \mathbf{A}_w + \lambda^2 \mathbf{R}^{-1})$ are both invertible, we have:

$$\begin{aligned}\mathbf{W}_w &= \mathbf{R} \mathbf{A}_w^H (\mathbf{A}_w \mathbf{R} \mathbf{A}_w^H + \lambda^2 \mathbf{I}_N)^{-1} = (\mathbf{A}_w^H \mathbf{A}_w + \lambda^2 \mathbf{R}^{-1})^{-1} \\ &\quad \times (\mathbf{A}_w^H \mathbf{A}_w + \lambda^2 \mathbf{R}^{-1}) \mathbf{R} \mathbf{A}_w^H (\mathbf{A}_w \mathbf{R} \mathbf{A}_w^H + \lambda^2 \mathbf{I}_N)^{-1} \\ &= (\mathbf{A}_w^H \mathbf{A}_w + \lambda^2 \mathbf{R}^{-1})^{-1} \mathbf{A}_w^H (\mathbf{A}_w \mathbf{R} \mathbf{A}_w^H + \lambda^2 \mathbf{I}_N)^{-1} \\ &\quad \times (\mathbf{A}_w^H \mathbf{A}_w + \lambda^2 \mathbf{R}^{-1}) \mathbf{R} \mathbf{A}_w^H. \quad [11]\end{aligned}$$

In the cost function, when no prior error term is considered (as in the case of traditional parallel MRI reconstruction (18,19)), the regularization parameter λ^2 is zero. Thus the inverse operator can be simplified as:

$$\mathbf{W}_w = (\mathbf{A}_w^H \mathbf{A}_w)^{-1} \mathbf{A}_w^H. \quad [12]$$

This is identical to the SENSE/SMASH reconstruction kernel (16,18,33). Note that the difference between underdetermined InI MRI and overdetermined parallel MRI is the incorporation of the prior error term in the cost function. The MNE of InI can be expressed in a form analogous to the previously derived prior-regularized parallel MRI reconstruction (30). One could also adopt the g -factor formulation from previous parallel MRI studies (18,30) to obtain the SNR ratio between fully sampled data and the dynamic InI.

Dynamic Statistical Parametric Map (dSPM)

Traditional dynamic MR image reconstruction provides time-resolved images. Subsequent statistical analysis on the time-series data yields SPMs. However, with InI we can normalize the reconstructed time-series image to the noise estimate to obtain SPMs at every time point. Using the linear inverse operator, the estimated variance of the noise at source location ρ is

$$\text{VAR}(\epsilon_\rho) = \langle (\mathbf{W}_{w,\rho} \mathbf{n}_w)(\mathbf{W}_{w,\rho} \mathbf{n}_w)^H \rangle = \mathbf{W}_{w,\rho} \mathbf{W}_{w,\rho}^H = \mathbf{W}_\rho \mathbf{C} \mathbf{W}_\rho^H, \quad [13]$$

where $\mathbf{W}_{w,\rho}$ and \mathbf{W}_ρ indicate the ρ -th row of \mathbf{W}_w , and \mathbf{W} , respectively.

A noise-normalized estimate of local image intensity power at location ρ is given by

$$f_\rho(t) = \frac{\text{VAR}(\hat{\mathbf{x}}_\rho(t))}{\text{VAR}(\epsilon_\rho)} = \frac{|\mathbf{W}_{w,\rho} \mathbf{y}'_w(t)|^2}{\mathbf{W}_{w,\rho} \mathbf{W}_{w,\rho}^H} = \frac{|\mathbf{W}_\rho \mathbf{y}'(t)|^2}{\mathbf{W}_\rho \mathbf{C} \mathbf{W}_\rho^H}. \quad [14]$$

Under the null hypothesis, $f_\rho(t)$ is F -distributed with one degree of freedom in the numerator and a large number of degrees of freedom in the denominator, which depends on the number of samples in the estimate of the noise covariance matrix. If a phase constraint is used (Eq. [1b]), the following dynamic statistics can be used to test the hypothesis about spin density to be either above or below the baseline:

$$z_\rho(t) = \frac{\hat{\mathbf{x}}'_\rho(t)}{\sqrt{\text{VAR}(\epsilon_\rho)}} = \frac{\mathbf{W}_{w,\rho} \mathbf{y}'_w(t)}{\sqrt{\mathbf{W}_{w,\rho} \mathbf{W}_{w,\rho}^H}} = \frac{\mathbf{W}_\rho \mathbf{y}'(t)}{\sqrt{\mathbf{W}_\rho \mathbf{C} \mathbf{W}_\rho^H}}. \quad [15]$$

By dividing the estimated spin density over the field of view (FOV) by the standard deviation (SD) of the estimated contaminating noise, $z_\rho(t)$ follows the t distribution under the null hypothesis of no spin density change ($\hat{\mathbf{x}}'(t) = 0$). When a large number of samples is used to estimate the noise covariance matrix, the t -distribution approaches the unit normal distribution. Thus $z_\rho(t)$ will be similar to the z -score.

Note that during derivation of the dynamic statistics, the prior information (\mathbf{x}_0) is not required. In other words, even without a static prior image, spatially-resolved dynamic changes can be obtained from the accelerated difference observations between experimental conditions. In practice, we can define a “baseline” period in the time-series experiment and calculate the differential data acquired with respect to the baseline. In this way, we rely only on the forward operator (and the associated inverse operator) to obtain spatially and temporally resolved statistical maps.

Analysis of Spatial Resolution

To quantify the spatial resolution in InI with MNE, we combine both the forward and inverse operators to form the resolution kernel:

$$\boldsymbol{\Psi} = \mathbf{W} \mathbf{A} = \mathbf{W}_w \mathbf{A}_w. \quad [16]$$

The columns of the resolution kernel specify the point spread function (PSF) for each source location (i.e., the spatial pattern of the estimated sources when a unit source is placed in a specific location). Similarly to MEG/EEG source analysis (34–36), we can employ the averaged PSF (aPSF) at location ρ to quantify the spatial spread of the InI MNE:

$$aPSF_{\rho} = \frac{\sum_{i,i \neq \rho} |d_{\rho}(i)| \psi_{i\rho}}{l}, \quad [17]$$

where $d_{\rho}(i)$ indicates the distance between source location i and source location ρ , $\psi_{i\rho}$ is the element from the i -th row and ρ -th column of the resolution kernel Ψ , and l is the number of voxels to be spatially resolved by InI. A map of the spatial distribution of the aPSF can be obtained by repeating the calculation across the whole source space.

MATERIALS AND METHODS

In this report we demonstrate how 1D InI can be used to reconstruct what would be the phase-encoding direction in conventional MRI. The FFT of a single k -space readout was used to obtain the spatial information from the frequency-encoding direction of a 2D image. The rationale for the 1D InI is to limit the source space within 1D phase-encoding direction by retaining the conventional use of the slice-selection and frequency-encoding gradients. This considerably decreases the degree of underdetermination in the InI reconstruction.

RF Coil Arrays

In this study we used a 23-channel and a 90-channel coil array (23) for a 1.5T scanner (Avanto; Siemens Medical Solutions, Erlangen, Germany). The 23-channel array was tiled from circular coils of 9.5-cm and 7.5-cm diameter. The 90-channel array consisted of 5.5-cm and 4.5-cm diameter coils. Both arrays used combinations of hexagonal and pentagonal symmetry with partial overlap between neighboring coils to minimize mutual inductance.

Experiment 1: InI Evaluation Using Simulated Data

To construct the source space and the forward operator in InI, we collected fully sampled (completely phase-encoded) coil sensitivity map images of a saline phantom using both the 23- and 90-channel coil arrays. These images were acquired with a gradient-echo sequence (TR = 10 ms, TE = 3 ms, flip angle = 10°, and 16 averages) on a 1.5T scanner. These coil sensitivity map images were low-pass-filtered with a 10-mm full width at half maximum (FWHM) isotropic Gaussian filter. Based on these data, we first performed a spatial resolution analysis using the aPSF described above.

To test InI in a dynamic imaging experiment, we used the canonical HDR waveform (37) with 30-s duration in a square region of interest (ROI; 5×5 voxels) to simulate the “signal” of InI acquisitions with contaminating “noise” using zero-mean unit-variance Gaussian distribution on individual images in each channel of the array. The SNR of the simulated data before spatial aliasing in the InI acquisitions was adjusted to different amplitude peak amplitude SNRs, which were parametrically varied from 0.2 to 10.

Experiment 2: Comparison of InI With Traditional EPI-Based BOLD fMRI

In Experiment 2 we used gradient encoding to reconstruct a conventional EPI-based fMRI time series. We also trun-

cated the acquisition to a single k -space line to simulate 1D InI.

Stimulus

For a visual fMRI experiment, a checkerboard stimulus was presented in a block-design paradigm using E-PRIME software (Psychology Software Tools, Inc., Pittsburgh, PA, USA). Each run consisted of an initial 64-s fixation period (“OFF”), an “ON” period of 64 s during which a circular checkerboard pattern reversing its contrast at 8 Hz was presented, and another 64-s “OFF” period. To increase the SNR, four runs were obtained for each subject in order.

Data Acquisition

Before the functional scans were performed, we acquired a structural spin-echo scan (59 3-mm-thick sagittal slices with $1 \text{ mm} \times 1 \text{ mm}$ in-plane resolution, covering the entire brain) to localize the position of subsequent scan planes (TR/TE = 600 ms/11 ms). In the functional scans we used single-shot gradient-echo EPI with the 23-channel array. The imaging parameters were as follows: TR = 1000 ms, TE = 40 ms, flip angle = 90°, slice thickness = 5 mm, FOV = $200 \text{ mm} \times 200 \text{ mm}$, image matrix = 64×64 , total = 192 measurements. To define the source space and forward operator needed in the InI reconstruction, coil sensitivity maps with a gradient-echo sequence (TR = 10 ms, TE = 3 ms, flip angle = 10°, FOV = $200 \text{ mm} \times 200 \text{ mm}$, image matrix = 64×64 , slice thickness = 10 mm, 16 averages, total acquisition time, 11 sec) were acquired. The coil sensitivity maps were averaged over 16 repeated scans to increase the SNR, at the cost of a minor increase in the total data acquisition time for the whole experiment.

Postprocessing and Data Analysis

To simulate InI acquisitions, only the central k -space line was retained and all other phase-encoding lines in the EPI raw images were discarded. The InI reconstruction algorithm provided time-resolved estimates of the functional changes and the associated dynamic statistical maps. Ten, five, or two neighboring time points were averaged in the simulation to quantify the dependency of InI reconstructions on SNR. As required for InI, coil sensitivity maps were estimated from the coil sensitivity map scan using the discrete wavelet transform algorithm (38).

All reconstructed time-series data were temporally detrended and spatially smoothed by a 6-mm FWHM isotropic Gaussian kernel. The percentage BOLD contrast was calculated by normalizing the time series signal to the average of the signal during the “OFF” condition. Using the general linear model (GLM), we calculated the t -statistics to reveal cortical regions that showed a statistically significant correlation with the experimental paradigm (39).

Experiment 3: InI Using 90-Channel BOLD fMRI

In Experiment 3 we acquired only the central k -space line using a principles of echo-shifting with a train of observations (PRESTO) echo-shifting scheme with TR = 20 ms (which is shorter than the TE = 43 ms needed for BOLD

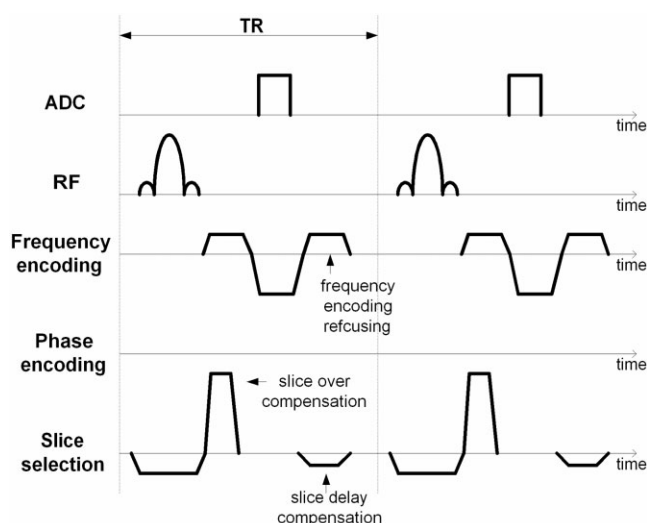


FIG. 1. PRESTO pulse sequence diagram in InI. PRESTO intentionally dephases the spin using an overcompensated slice-selection gradient during RF excitation. Before the end of the TR, a delay compensation gradient is employed to shift the echo to the next TR. This example illustrates a TE with a 4-TR delay PRESTO.

contrast.) The 1D InI method was used to reconstruct a time series with 20-ms temporal resolution such that the right-left spatial direction was obtained from the FFT of the readout line (conventional frequency encoding), and the anterior-posterior direction's spatial information was obtained from the detector distribution.

Stimulus

The same visual checkerboard stimulus described above for Experiment 2 was used. However, to mitigate a data-throughput issue in the current implementation, we adjusted the total duration of a run to 56 s, involving an 8-s OFF, a 32-s ON, and a 16-s OFF period.

Pulse Sequence

In MR InI, spatially encoded data from the RF coil array can be acquired with a very short TR (<10 ms). With classic steady-state-incoherent (SSI) fast imaging techniques (26), such as EPI or spiral imaging, TEs longer than the TR cannot be obtained. This is particularly challenging for BOLD and other experiments that require long TEs to build up the dynamic contrast. To overcome the difficulty imposed by the constraint of $TR > TE$ in SSI sequences, we

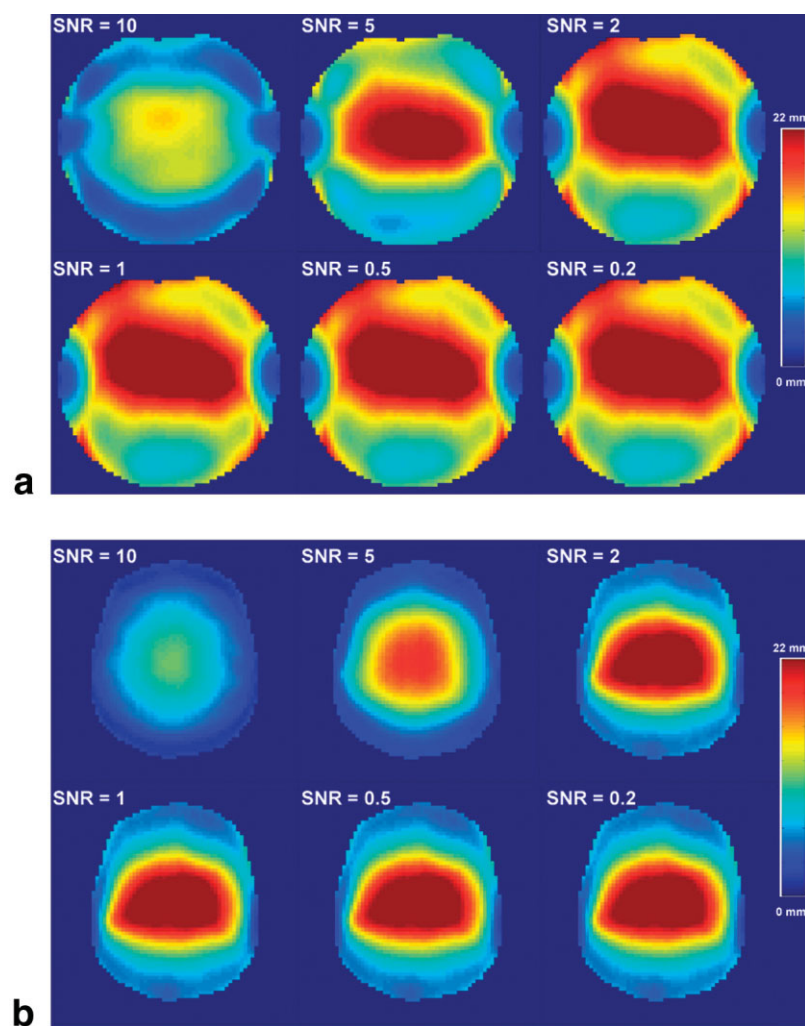


FIG. 2. aPSF for a 23-channel array (a) and a 90-channel array (b) at different peak SNRs, as indicated. The aPSF increases progressively as the acceleration rate increases. [Color figure can be viewed in the online issue, which is available at www.interscience.wiley.com.]

Table 1
The Average (Avg.), Standard Deviation (SD) and Maximum (Max.) of the Averaged Point-Spread Function (aPSF) from 23-Channel Array and 90-Channel Array at Different Peak SNR

SNR	aPSF (mm)					
	90-channel			23-channel		
	Avg.	SD	Max.	Avg.	SD	Max.
0.2	12.0	6.8	26.6	15.6	5.9	28.3
0.5	12.0	6.8	26.6	15.6	5.9	28.3
1	12.0	6.8	26.6	15.6	5.9	28.3
2	11.8	6.8	26.3	15.5	5.9	28.1
5	8.6	5.2	25.3	12.7	5.4	24.7
10	5.2	2.8	11.1	7.8	3.4	14.8

used another steady-state fast imaging technique, the PRESTO sequence (40). Specifically, we used the slice-selection gradient to shift the TE by various multiples of TR and obtain a TE > TR. This sequence is shown in Fig. 1. We implemented a PRESTO sequence with TR = 20 ms, including RF excitation, off-resonance slice-selection gradient, frequency-encoding prephase, slice-selection prephase, and frequency-encoding readout. Before the end of each TR, the frequency-encoding compensation gradient refocused the magnetization in frequency-encoding direction. Also, at the end of each TR, a slice-selection compensation gradient refocused part of the off-resonance slice-selection during RF excitation to enable the prolonged TE in the next TR. The first moment of the slice-selection compensation gradient was adjusted to shift TE by two TR periods, resulting in TE = 43 ms. In the MR InI with PRESTO sequence, no phase-encoding gradients were used.

Data Acquisition

fMRI data were collected using the 90-channel coil array. Before each functional scan session a structural spin-echo sagittal scan with 5.93-mm-thick slices and 1 mm × 1 mm in-plane resolution covering the entire brain was acquired to localize the position of subsequent scan planes (TR/TE = 600 ms/11 ms). Using the PRESTO sequence, we collected ultrafast MR InI acquisitions with TR = 20 ms, flip angle = 20°, TE = 43 ms, FOV = 200 mm × 200 mm, and slice thickness = 5 mm. A total of 3000 images were acquired in 60 s, including 4 s of dummy scans to reach the

steady state, and 56 s for the fMRI experiment. The experiment was repeated 20 times. Similarly to Experiment 2, an additional scan was performed to estimate the coil sensitivity map required in InI reconstruction.

Postprocessing and Data Analysis

The time courses from all channels of the RF coil array were detrended and averaged across experiments to improve the SNR. After InI reconstruction, spatial smoothing was implemented by means of a 6-mm FWHM isotropic Gaussian kernel. We defined the baseline as the 24-s interval in the “OFF” condition, and calculated the dynamic *t*-statistics maps with 20-ms temporal resolution. The required coil sensitivity maps in InI reconstruction were estimated using a discrete wavelet transform based on the coil sensitivity map scan (38). All image reconstructions were performed on a Pentium-4 2GB dual processor Linux system with code written in MATLAB (Mathworks, Natick, MA, USA).

RESULTS

Experiment 1: InI Evaluation Using Simulated Data

Figure 2a shows the aPSF for the 23- and 90-channel arrays. Note that for both coil arrays the aPSF decreased as the SNR increased from 0.2 to 10. Table 1 lists the average, SD, and maximum values of the aPSF for both RF coil arrays at different SNRs. For both arrays the aPSF increased when the SNR decreased from 10 to 0.2. For SNR < 1, the aPSF of a given RF coil array no longer depended on SNR. This may reflect the fact that a high regularization parameter was required for the inverse operator in the low-SNR case, and thus the aPSF was dominated by the noise covariance matrix rather than the forward operator. Thus, lower SNR increased the dependency on regularization, in agreement with a previous MEG source localization analysis (41). One feature common to both the 23- and 90-channel arrays is that the aPSF is larger at the center of the FOV than at the periphery of the FOV. This is likely due to the lower array element sensitivity at the center of the FOV and the increased breadth of coil sensitivities at the center of the FOV. A similar increased central aPSF was observed in a study of MEG/EEG source localization using MNE (35). For brain imaging, this indicates that dynamic changes originating from deep-brain structures will be spatially blurred in InI

Table 2
The Average (Avg.), Standard Deviation (SD) and Maximum (Max.) of the Averaged Point-Spread Function (aPSF) from the 90-Channel Array With Progressively Added Phasing Encoding Lines at Different Peak SNR

SNR	aPSF (mm)											
	r = 64			r = 32			r = 16			r = 8		
	Avg.	SD	Max.	Avg.	SD	Max.	Avg.	SD	Max.	Avg.	SD	Max.
0.2	12.0	6.8	26.6	6.0	3.4	13.3	3.0	1.7	6.8	1.5	0.8	3.7
0.5	12.0	6.8	26.6	6.0	3.4	13.3	3.0	1.7	6.8	1.5	0.8	3.7
1	12.0	6.8	26.6	6.0	3.4	13.3	3.0	1.7	6.8	1.5	0.8	3.7
2	11.8	6.8	26.3	5.8	3.3	13.0	2.8	1.6	6.5	1.3	0.8	3.2
5	8.6	5.2	5.3	3.8	2.2	8.2	1.6	0.9	3.6	0.7	0.4	1.6
10	5.2	2.8	11.1	2.4	1.3	4.7	1.1	0.5	2.2	0.3	0.3	0.8

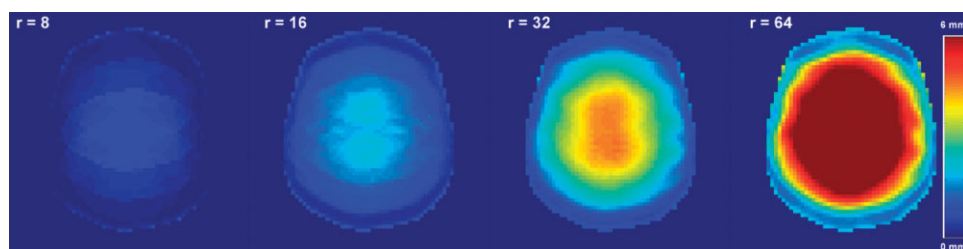


FIG. 3. aPSF for a 90-channel array at peak SNR = 10 with different acceleration rates. As acceleration rates progressively increase from eightfold to 64-fold, the aPSF increases.

reconstructions. When we compared the 23- and 90-channel results, we found that the aPSF for the 90-channel array was smaller, suggesting higher spatial resolution of

the reconstructions, presumably due to the presence of more spatially independent information available from the 90-channel RF coil array.

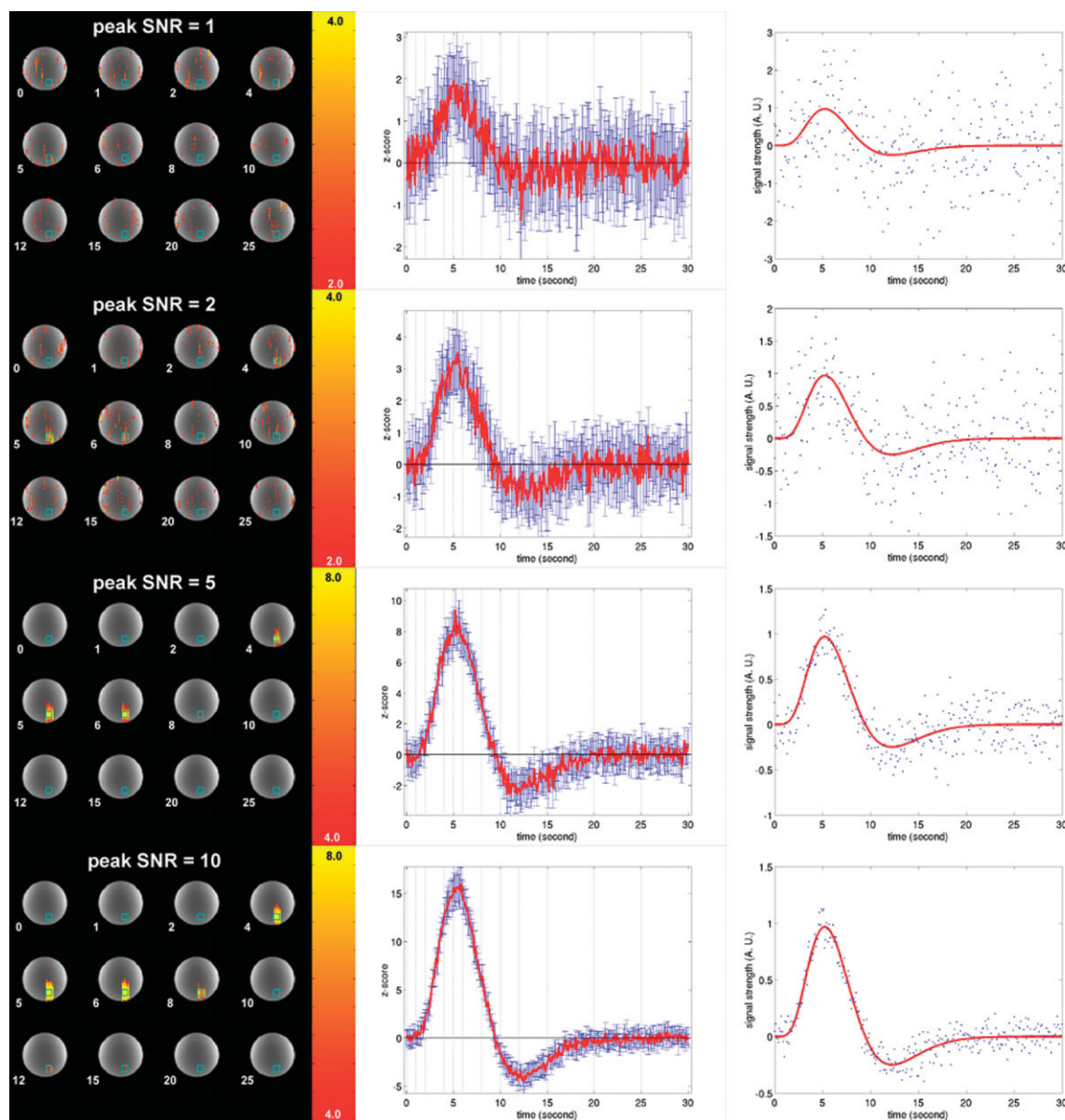


FIG. 4. dSPM of MR Inl from the simulated HDR with different peak SNRs. Left panels: Snapshots of the absolute value of the t -statistics maps are shown at different time points, indicated by the lower-left corner numbers (in seconds). The blue square indicates the ROI of the simulated HDR. Middle panels: Averaged t -statistics time courses within the simulated ROI. The blue error bars show the SD within the ROI. The light gray vertical lines indicate the time points of the snapshot shown in the left panel. Right panels: One realization of a simulated canonical HDR time course with noise at different peak SNRs (blue dots). The red trace is the simulated HDR signal without noise.

As a generalization of parallel MRI, InI can employ progressively more phase-encoding steps to approach classic SENSE reconstruction. Figure 2b shows the aPSF for the 90-channel array with peak SNR = 10 as the acceleration rate increases from $r = 4$ to $r = 64$. Table 2 lists the aPSFs from the 90-channel array coil when the acceleration rate r was decreased from 64-fold (one k -space line) to eightfold (eight k -space lines). Note that more phase-encoding steps suppressed aPSF gradually. Again, lower SNR corresponded to larger aPSF. Figure 3 illustrates the progressive changes of aPSF as the acceleration rate changes from eight- to 64-fold. The aPSF at the center of the FOV increases more rapidly than at the periphery of FOV as the acceleration rate increases.

To simulate dynamic imaging, we created canonical HDRs of 30-s duration with peak SNRs of 1, 2, 5, and 10. Figure 4 shows the realizations of these HDRs. The InI t -statistics time-series reconstructions are also shown in Fig. 4. For the case of high SNR (SNR = 10), InI provided dynamic statistical inference with good spatial localization, particularly between 4 and 8 s. Even at the 12-s post-stimulus undershoot, InI detected statistically significant activation in the simulated ROI. The time courses within the ROI in the InI reconstructions matched well to the simulated HDR with contaminating noise. As SNR dropped from 10 to 1, we observed a gradual degradation of localization precision. At SNR = 5, the localization was still within the simulated ROI. Low SNR (SNR = 2 and 1) resulted in more false-positives.

Experiment 2: Comparison of InI With Traditional BOLD fMRI Acquisitions

Figure 5 shows a t -statistics map from the 23-channel visual fMRI experiment. A strong activation was found in the occipital lobe. The time course of the BOLD contrast within the statistically significant ROI was also shown. The maximum BOLD contrast was approximately 3% in this experiment. To simulate InI acquisitions, only the central k -space line was kept and all other lines were discarded. These InI reconstructions are shown in Fig. 6. To test the dependency of InI reconstructions on SNR, we averaged 10, five, or two subsequent time points in the reconstructed data. In all cases, occipital activation was seen. The SNR was improved when more time points were averaged. Nevertheless, even with only two-timepoint collapsed dSPMs, consistent occipital lobe activation was found in InI dSPMs at “ON” time points.

Experiment 3: InI Using 90-Channel BOLD fMRI

Using a PRESTO sequence and the 90-channel array at 1.5T, we performed BOLD fMRI at 20-ms temporal resolution (TR = 20 ms) with TE = 43 ms. Coil sensitivity profiles in a single plane from all channels in the RF array are shown in Fig. 7. Using InI reconstructions, we generated 2800 dSPMs. Figure 8 shows snapshots of “ON” and “OFF” reconstructions, illustrating the quality of InI reconstructions. We selected two ROIs (one in the temporal lobe and one in the occipital lobe) to examine the time course of the InI estimates. Figure 9 shows the averaged time courses at these two ROIs. Elevated dynamic change estimates during the “ON” condition were found in the

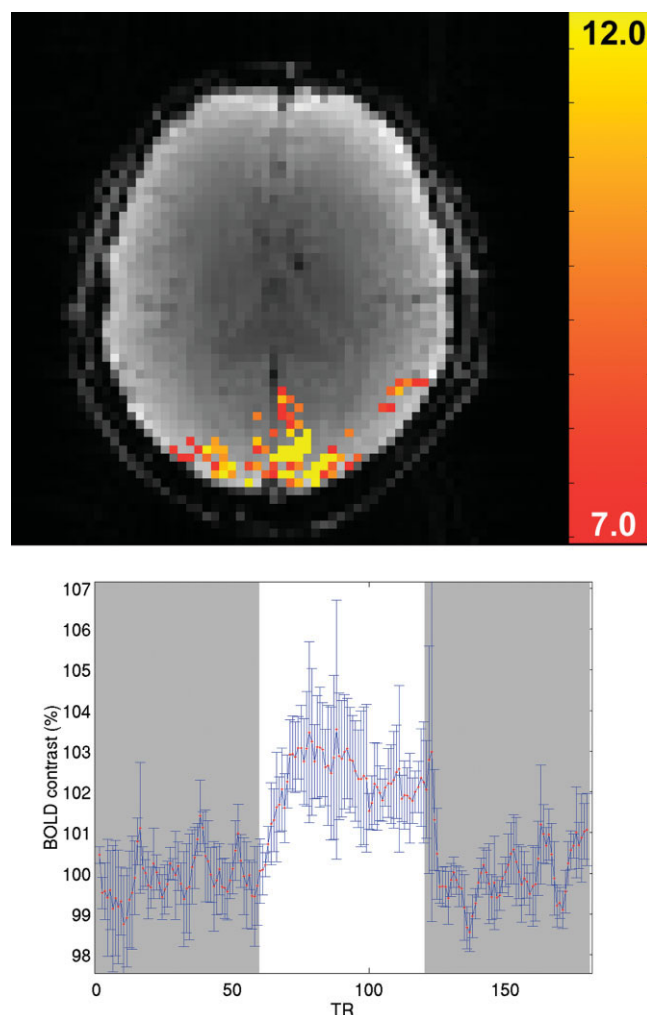


FIG. 5. Top: A t -statistics map of brain activation observed in a 23-channel visual fMRI experiment with block-design flickering checkerboard stimulation. Bottom: The BOLD contrast time course, in percentage with respect to baseline. The red dots are the mean of the ROI defined by the t -statistics larger than 7.0, and the blue error bars indicate SDs. [Color figure can be viewed in the online issue, which is available at www.interscience.wiley.com.]

occipital lobe ROI, in contrast to the oscillatory time courses around the baseline in both “ON” and “OFF” conditions in the temporal lobe ROI (likely from cardiac and respiratory modulations). Figure 10 shows side-by-side MNE and dSPMs of three representative segments of the experiment, including one baseline period and two checkerboard flashing periods. Note that during baseline MNE can reconstruct time-series images with physiological modulation, while there is no statistically significant activation across the whole FOV. During checkerboard flashing, strong dynamic changes were identified around the back of occipital lobe by MNE, and accordingly dSPMs showed statistically significant functional activation around the visual cortex. The averaged time-resolved t -statistics over the occipital lobe ROI are also shown at 20-ms temporal resolution in Fig. 11. We observed a clearly elevated statistical significance level during visual stimulation. We also clearly resolved oscillations that followed the cardiac and respiratory cycles.

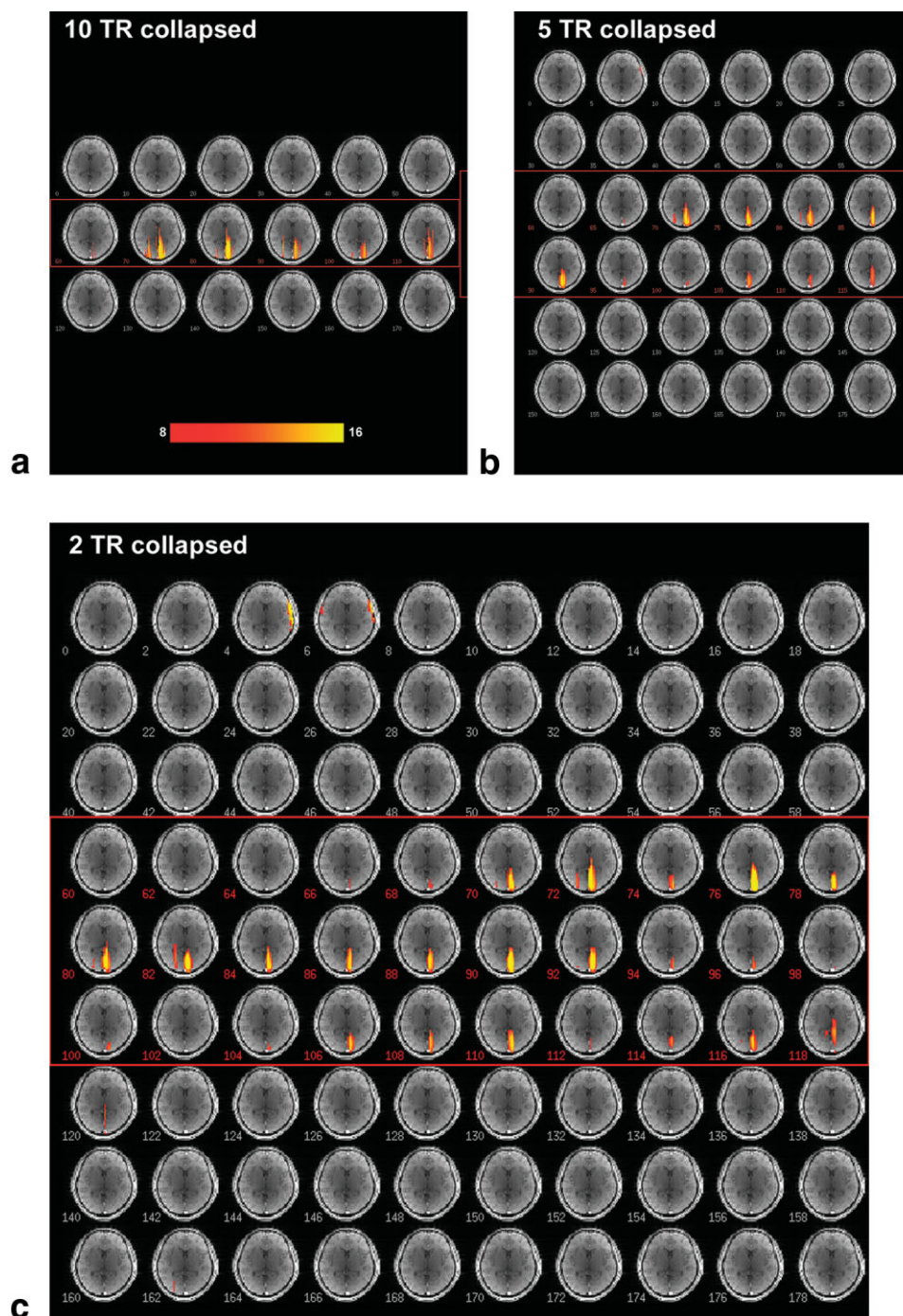


FIG. 6. MR InI dynamic F-statistics maps using decimated 23-channel visual BOLD fMRI data. To increase SNR, we sacrificed temporal resolution by averaging neighboring two (a), five (b), or 10 (c) time points. The dSPMs showed statistical significant activations in the occipital lobe. The red box indicates the time points at which the visual stimulus was presented ("ON").

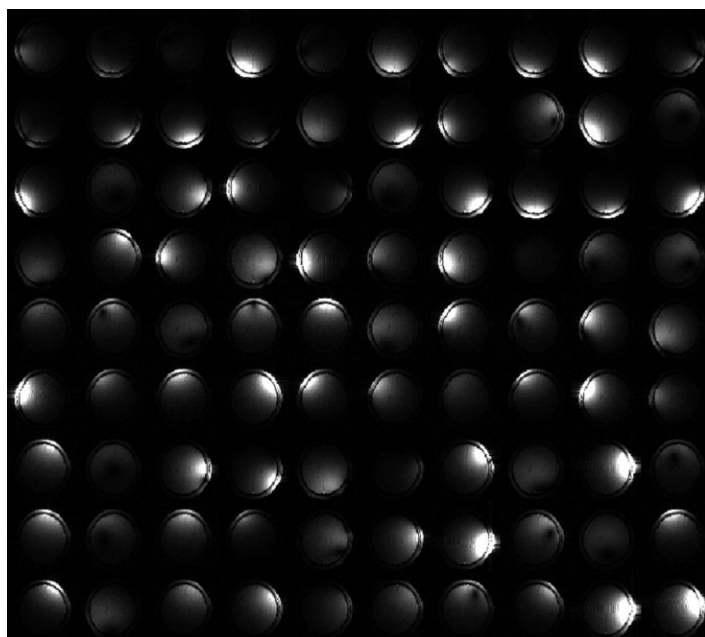
DISCUSSION

The proposed MR InI framework provides a methodology to obtain fast MRI acquisitions with a temporal resolution in the millisecond range. In particular, we expect that InI can be applied to dynamic imaging for improved characterization of temporal evolution of MR signals. The InI approach can be used to investigate any potential MR contrast mechanism with buildup and washout time on the millisecond scale. We expect that, equipped with this

high temporal resolution, investigators will be able to identify credible dynamic changes by using optimized InI contrast-mechanism preparations, data-acquisition procedures, and image-reconstruction algorithms.

Traditional MR experiments consist of two steps: MR contrast preparation and MR data acquisition. InI attempts to improve the temporal resolution in the data-acquisition step. In InI, the spatial resolution is not derived from gradient switching, as in Fourier imaging (26), but rather

FIG. 7. The coil sensitivity map images from a 90-channel RF coil array. Disparate spatially localized sensitivity was observed in different channels.



from the B_1 field distribution from multiple channels in the RF coil array. As described in the Theory section, InI involves solving a 1D, 2D, or 3D inverse problem. In contrast to MEG and EEG source localization, which is intrinsically a 3D inverse problem, MR InI can utilize slice-selection and frequency-encoding gradients to substantially decrease the degree of uncertainty without much compromise in the temporal resolution. Using modern gradient technology, 64 frequency-encoding steps can be accomplished within 0.5 ms (2K bandwidth). In addition, the slice-selection and RF excitation typically take up to a few milliseconds in most sequences. In theory, with appropriate modification of the MR contrast preparation, InI can be applied to different pulse sequences and anatomical regions for high-temporal-resolution imaging.

Since the spatial resolution of InI depends significantly on the spatial information from channels in the RF coil array, it

is expected that introducing more independent spatial information into the coil array, such as by increasing the number of channels, or using another RF coil design to introduce higher B_1 variability, will improve the spatial resolution. Indeed, as documented in the MEG source localization literature, increasing the number of sensors (analogously to the number of channels in the RF coil array in MRI) contributes to increased spatial resolution (25).

As expected, the spatial resolution in the InI-reconstructed direction was worse than that in Fourier imaging. However, since no phase-encoding step was introduced, the bandwidth in the phase-encoding direction was infinite. This is in contrast to EPI, which suffers from low acquisition bandwidth in the phase-encoding direction. Since only frequency encoding is used, the geometrical distortions due to B_0 susceptibility effects are minimal in the InI method.

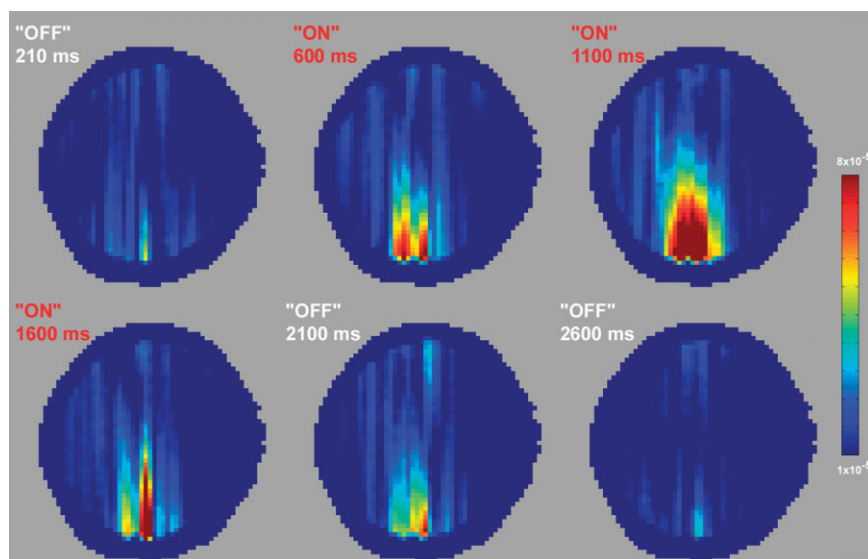


FIG. 8. Snapshots of InI reconstructions before averaging during "ON" and "OFF" conditions, respectively. The images are shown in arbitrary units. [Color figure can be viewed in the online issue, which is available at www.interscience.wiley.com.]

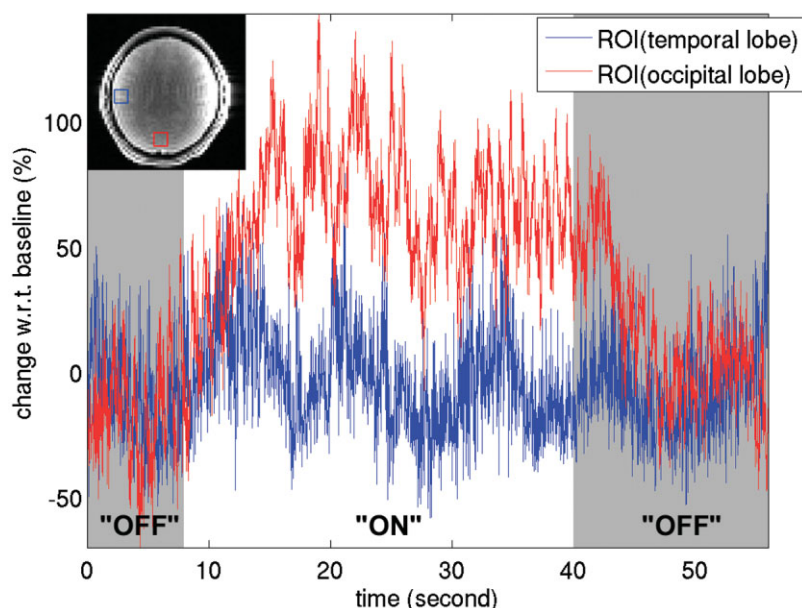


FIG. 9. Averaged time courses within an ROI in the temporal (blue) and occipital (red) lobes in InI-reconstructed dynamic change estimates. [Color figure can be viewed in the online issue, which is available at www.interscience.wiley.com.]

Here InI was explicitly derived as a generalization of parallel MRI. Thus, within the unified InI framework, one can choose the degree of uncertainty in image reconstruction from an overdetermined system in classic parallel MRI, including SENSE, SMASH, and GRAPPA, to an underdetermined system in extremely accelerated InI. The trade-off between these two is the required spatiotemporal resolution in versatile applications. Parallel MRI can restore the spatial resolution and accelerate the data acquisition at a modest rate, which is usually limited by the number of channels in the RF coil array. InI, on the other hand, sacrifices spatial resolution for massive speedup. Overall, InI provides more flexibility for trade-offs between the spatial and temporal resolution.

In InI and traditional parallel MRI, the acceleration rate r is calculated as the ratio between the number of k -space data to be reconstructed and the number of acquired k -space data. In fact, the numbers of columns and rows in a whitened forward operator \mathbf{A}_w reflects the acceleration rate, given the number of channels in an RF coil array. When r is small in traditional parallel MRI acquisitions/reconstructions, \mathbf{A}_w has more rows than columns, and the rank of \mathbf{A}_w depends on the column dimension. This indicates that more spatial information is provided from channels of an RF array (row dimension) to resolve a full-FOV image (column dimension). As r increases, k -space sampling decreases and \mathbf{A}_w decreases the row dimension accordingly. Further increase of r leads to a transition point where the rank of \mathbf{A}_w depends on the row dimension, instead of the column dimension. This transition point indicates that the information encoded in \mathbf{A}_w is limited by the number of channels in the RF coil array. Beyond this transition, r can be even further increased by expanding the columns dimension of \mathbf{A}_w , corresponding to a source space of higher spatial resolution. However, since the available information is limited by the row dimension of \mathbf{A}_w , the spatial resolution of the reconstructed image cannot be further improved by specifying a higher-spatial-resolution source space.

Since only the central k -space line is acquired in InI, the number of rows of \mathbf{A}_w (the number of the channels in an RF coil array times the number of acquired k -space lines) is usually smaller than the number of columns (the size of source space). Thus InI reconstruction involves an underdetermined linear system. However, by using coarser specification of the source space or acquiring more k -space lines, one can turn the reconstruction into an overdetermined linear system. As described in the Theory section, one can control the transition between solving under- and overdetermined linear equations by incorporating a regularization parameter and a prior term in the cost function.

One major feature of InI is that no prior image is necessary to obtain spatially resolved dSPMs. This is because in dynamic imaging we focus on localizing the changes over the experiment interval, rather than reconstructing the time-resolved images themselves. In traditional functional brain imaging, usually a time series of a fully phase-encoded image is acquired, and statistics are subsequently calculated. In contrast, the computation of statistics inference and the image reconstruction are integrated in InI. Even without a full-FOV prior image, InI can restore full-FOV time-resolved t -statistics or F -statistics maps using the spatial information encoded in an RF coil array. If a credible prior image is provided, InI can generate time-series images with both dynamic change estimates and underlying stationary anatomy. InI's ability to reconstruct estimates and associated statistics of dynamic changes without a prior static image distinguishes it from prior-informed regularized parallel MRI (20,30) or other prior-information-based imaging approaches (11,42). In fact, one could also apply the derived dSPM formula in InI to other dynamic MRI reconstructions by utilizing a linear inverse operator to restore full-FOV dynamic changes without a prior image.

Here we would like to clarify the distinction between the coil sensitivity map images and the prior image in InI. The purpose of the coil sensitivity image in InI is to provide the estimate of coil sensitivity maps for the RF coil

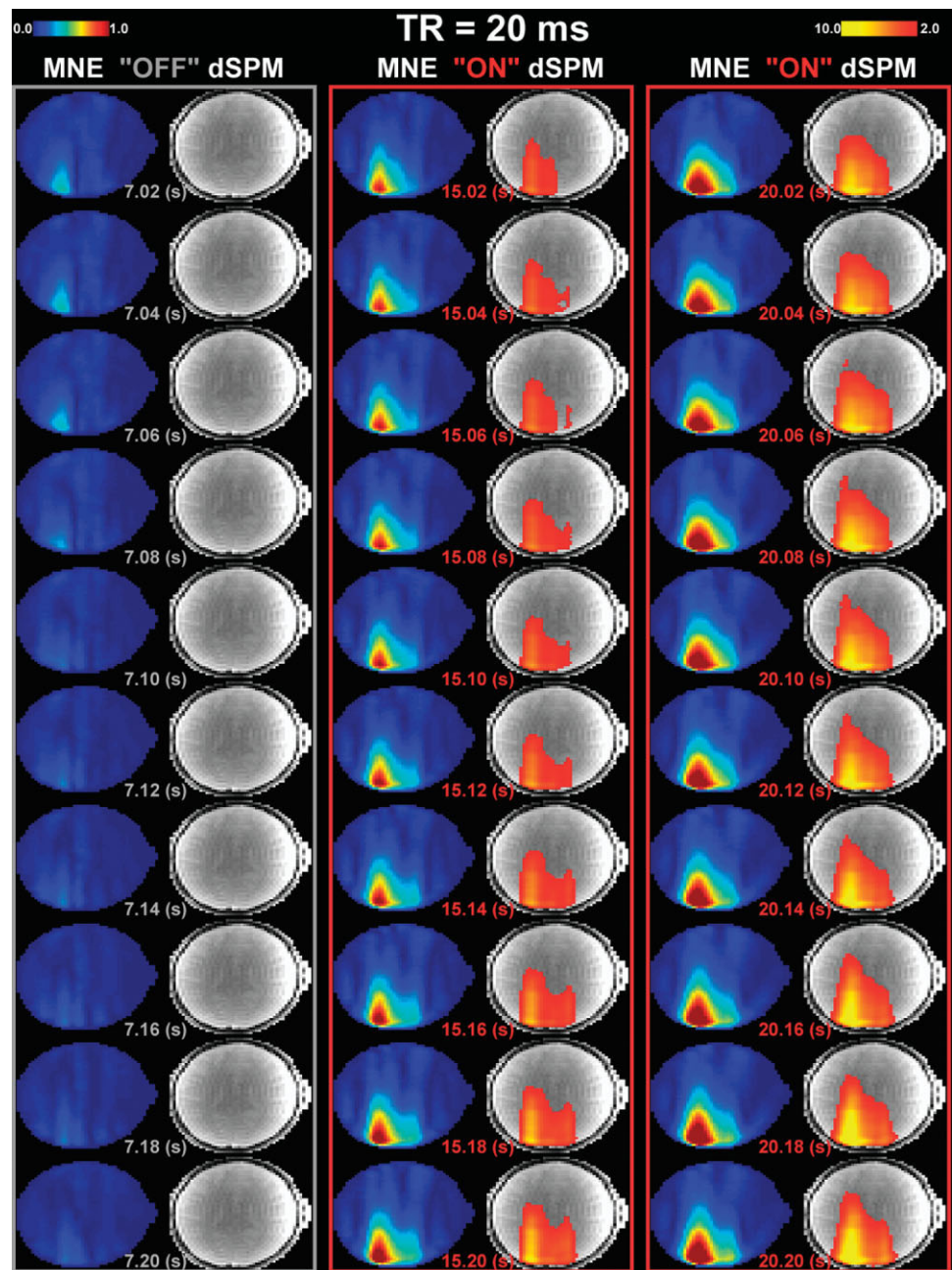


FIG. 10. Snapshots of pairs of InI MNE and dSPMs during one baseline period and two checkerboard flashing periods. The time points for each snapshot are marked at the center bottom for each reconstruction pair. Strong localized functional activation and associated statistics are seen in the occipital lobe during the “ON” condition.

array. This is common to all parallel MRI reconstruction algorithms. The purpose of a prior image, on the other hand, is to generate the full-FOV reconstructed image dynamically for visualization by adding a stationary image to the dynamically reconstructed images. Without a prior image, time-resolved full-FOV images, including both stationary anatomical features and dynamic functional changes, cannot be generated. Nevertheless, since the prior image does not contribute to the reconstruction of dynamic changes, full-FOV dynamic statistical maps can still be generated. Taking brain fMRI as an example, providing a prior image can generate the time series of full-FOV brain images with both anatomical features and BOLD contrast, whereas without a prior image, only statistical maps can be calculated by InI reconstruction algorithm. Thus,

whether the underlying stationary full-FOV image with anatomical features is desired depends on the application involved.

In InI, a regularization parameter is employed to stabilize the matrix inversion in the derivation of the inverse operator. A large λ^2 penalizes the activation and biases the MNE toward the baseline activity. On the other hand, if λ^2 is too small, the inverse operator may become unstable because $\mathbf{A}_w \mathbf{R} \mathbf{A}_w^H$ can be ill-conditioned due to strong correlations among channels in an RF array, and subsequently the matrix inversion required to derive the inverse operator will be sensitive to amplified noise. It is crucial to achieve a proper trade-off between these two ends in order to find an optimal regularization parameter to achieve sensitivity for activation detection and robustness of the

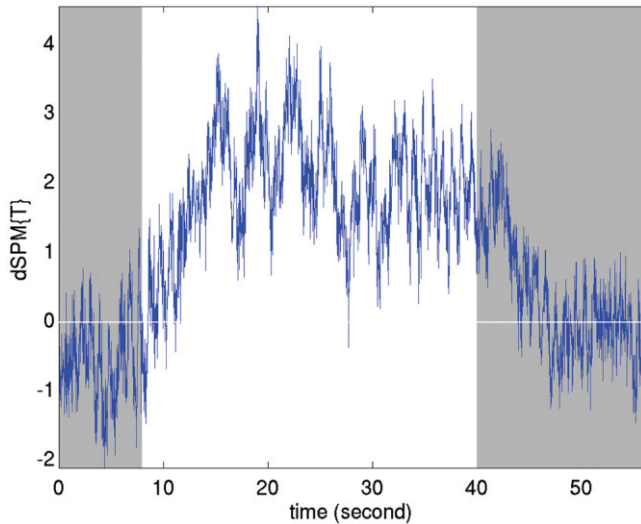


FIG. 11. Averaged BOLD fMRI t -statistics time course of 20-ms temporal resolution within an occipital-lobe ROI. The shading indicates the “OFF” condition. Elevated statistical significance values were observed during the “ON” condition (white). [Color figure can be viewed in the online issue, which is available at www.interscience.wiley.com.]

inverse operator simultaneously. Potentially, this could be done with the use of algorithms, such as L-curve (30,31) or generalized-cross-validation (43). To illustrate the impact of a chosen regularization parameter, Fig. 12 shows reconstructed InI t -statistics maps utilizing different regularization parameters. Note that with a small λ^2 (1% of the estimated λ_0^2 as described in the Theory section), InI is not sensitive to detect activation, possibly because of amplified noise from the inverse operator. However, with a large λ^2 ($100 \lambda_0^2$), more falsely positive activation was estimated at the same threshold. This is likely because of overly suppressed noise estimates in the baseline compared to the suppressed noise in InI reconstruction at all time points. This result illustrates the importance of choosing an appropriate regularization parameter in InI reconstruction to optimize detection power. Interestingly, we found

that InI reconstructions using regularization parameters of $100 \lambda_0^2$ and λ_0^2 both detected significant activation in the ROI containing the synthetic HDR. The insensitivity of dSPMs to large regularization parameters can be derived from the expression of the inverse operator in Eq. [9]. The second part of the inverse operator, $(\mathbf{A}_w \mathbf{R} \mathbf{A}_w^H + \lambda^2 \mathbf{I}_N)^{-1}$, is more dominated by the identity matrix as the regularization is large, which may be our cases of $100 \lambda_0^2$. The insensitivity of localization accuracy to the regularization parameter in the low-SNR case was previously reported in an MEG study (41). Again, a full investigation into the choice of the regularization parameter is necessary in order to optimize the InI reconstruction.

A high value of the regularization parameter leads to an inverse operator suppressing the amplitude of MNE (see Eq. [9]). However, calculating statistical maps by taking a ratio between the MNEs of activation and noise level may show a strong dependence on the transpose of whitened forward operator (Eq. [9]). Thus the localization accuracy is strongly determined by the whitened forward operator itself.

The image reconstruction procedure makes the InI experimental design similar to MEG and EEG experiments. In InI, we need to define a baseline interval in order to detect dynamic change and statistical inference normalization. The baseline can be an interval before the presentation of the stimulus, as is commonly used in MEG/EEG evoked-response experiments. Since baseline data are used to subtract the measurements during the condition of interest, in the context of InI, signal levels actually contrast between the two conditions.

The localization accuracy of InI critically depends on the SNR. Similarly to MEG/EEG experiments, one can improve the SNR by averaging the data from repeated trials. Another similarity between MEG/EEG and InI is that InI has lower spatial resolution around the center of the head. Thus, if InI is applied to brain imaging, the dynamic changes in deep-brain areas will be spatially blurred. Since spatial resolution depends on the SNR, we would expect substantial improvements in the PSF from higher field acquisitions (or any other method that increases SNR, such as trial averaging). In addition, as described in the

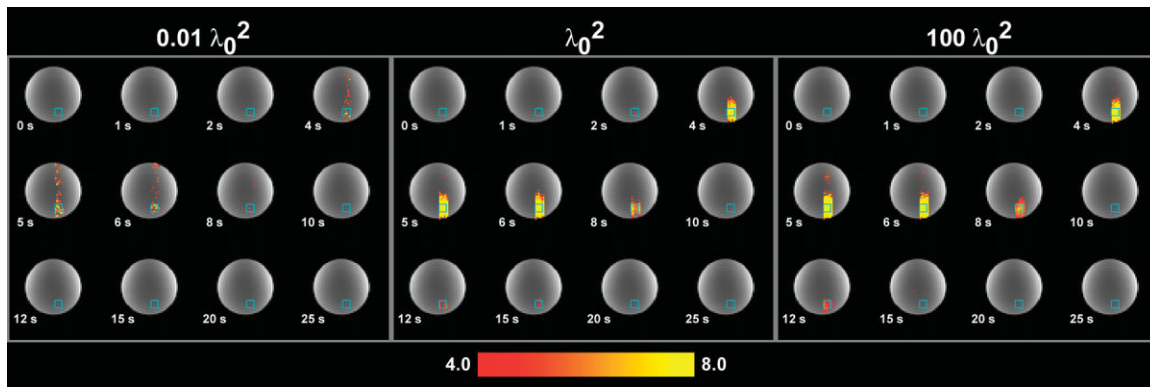


FIG. 12. dSPMs of MR InI from the simulated HDR with different peak SNRs using different regularization parameters. λ_0^2 is the regularization parameter estimated in this paper. Snapshots of the absolute value of t -statistics maps at different time points are indicated by the lower-left corner numbers (in seconds). The blue square indicates the ROI of the simulated HDR. [Color figure can be viewed in the online issue, which is available at www.interscience.wiley.com.]

Theory section, a limited amount of phase-encoding can further improve the spatial resolution.

Besides SNR, the spatial resolution of InI also depends on the B_1 field distribution. InI uses the spatial information encoded in an RF coil array to resolve the spatially collapsed signals into a full-FOV image. The amount of independent information encoded in B_1 fields thus determines the ultimate spatial resolution in InI reconstructions. At deep regions in the FOV (away from the RF coil array), the B_1 field may be too smooth to resolve neighboring sources, due to the inherent smoothness of electromagnetic fields far from the coils. Thus, like parallel MRI, we expect that the spatial resolution in InI will ultimately be limited by the distribution of the electromagnetic fields from the channels in the RF coil array. In this study, this phenomenon was demonstrated in the larger PSF at the center of the FOV for both 23- and 90-channel coil arrays. We expect that the spatial resolution of InI can be improved at high field because of the shorter wavelength. Compared to other parallel MRI acquisitions, InI is expected to suffer more seriously from limited spatial resolution because no phase-encoding is employed.

In this study InI was used in conjunction with a PRESTO sequence to acquire BOLD hemodynamic contrast. In the context of InI, a pulse sequence with $TE > TR$ is indispensable for optimal BOLD contrast, which requires TE approximately equal to T_2^* . At field strengths of 1.5–7T, the T_2^* ranges between 20 ms and 50 ms in brain parenchyma. The echo-shifting technique allows the TE to be tens of milliseconds while it suppresses the TR to be less than 10 ms. PRESTO is one realization of this method.

In fast imaging (e.g., EPI and spiral imaging methods), physiological effects from peripheral nerve stimulation, the specific absorption rate (SAR), and acoustic noise often limit the speed of the acquisition. In general, InI greatly reduces these limitations. The nerve stimulation hazard can be mitigated by InI compared to spiral or EPI methods because a relatively low-amplitude, long readout is used without switching the gradient polarity. One can achieve a further reduction in nerve stimulation by discarding frequency encoding and using 2D InI, in which case only the slice-selection gradient is employed. The high temporal resolution limits SAR exposure by reducing the excitation flip angle to the Ernst angle, which for TR s of tens of milliseconds is considerably lower than for conventional EPI or spiral acquisitions. Since SAR scales linearly with the duty cycle but quadratically with the RF pulse peak power (amplitude), SAR is substantially reduced and becomes similar to that of typical low-flip-angle gradient-echo sequences. The challenge of acoustic noise is common in EPI-based fMRI studies. The source of such acoustic noise is the gradient switching required in the high-bandwidth EPI readouts. One can reduce this artifact by greatly reducing the readout bandwidth in 1D InI or eliminating the readout entirely in 2D InI.

Respiratory and cardiac rhythms may confound the time course of dynamic InI. In fact, these are two common sources of physiological noise in fMRI experiments (44). With a temporal resolution about 1 s, temporal aliasing makes it difficult to remove these modulations in conventional BOLD experiments. Since InI allows fast acquisition of dynamic scans, the physiological signals are adequately

sampled without aliasing, thus potentially allowing better removal of these confounding effects.

CONCLUSIONS

We have introduced an MR InI methodology to improve the temporal resolution of dynamic MR measurements on the millisecond scale. Using information from multiple channels in the RF coil array, InI can spatially resolve dynamic changes with statistics by solving an inverse problem. This is analogous to MEG/EEG source localization. InI is a generalization of parallel MRI. We validated the InI method using 23- and 90-channel RF coil array simulations. In addition, we measured a BOLD hemodynamic fMRI response to visual stimulation at 20-ms temporal resolution. The proposed InI method can be flexibly applied to other MR contrast mechanisms and anatomical regions for variable spatiotemporal resolutions based on variants of InI source-space specification, data-acquisition schemes, and image-reconstruction algorithms.

ACKNOWLEDGMENTS

We thank Dr. Graham Wiggins for developing the RF coil arrays used in this study.

REFERENCES

1. Belliveau JW, Rosen BR, Kantor HL, Rzedzian RR, Kennedy DN, McKinstry RC, Vevea JM, Cohen MS, Pykett IL, Brady TJ. Functional cerebral imaging by susceptibility-contrast NMR. *Magn Reson Med* 1990; 14:538–546.
2. Ogawa S, Lee TM, Kay AR, Tank DW. Brain magnetic resonance imaging with contrast dependent on blood oxygenation. *Proc Natl Acad Sci USA* 1990;87:9868–9872.
3. Belliveau JW, Kennedy Jr DN, McKinstry RC, Buchbinder BR, Weisskoff RM, Cohen MS, Vevea JM, Brady TJ, Rosen BR. Functional mapping of the human visual cortex by magnetic resonance imaging. *Science* 1991;254:716–719.
4. Kwong KK, Belliveau JW, Chesler DA, Goldberg IE, Weisskoff RM, Poncelet BP, Kennedy DN, Hoppel BE, Cohen MS, Turner R, Cheng H, Brady TJ, Rosen BR. Dynamic magnetic resonance imaging of human brain activity during primary sensory stimulation. *Proc Natl Acad Sci USA* 1992;89:5675–5679.
5. Logothetis NK, Pauls J, Augath M, Trinath T, Oeltermann A. Neurophysiological investigation of the basis of the fMRI signal. *Nature* 2001;412:150–157.
6. Bodurka J, Bandettini PA. Toward direct mapping of neuronal activity: MRI detection of ultraweak, transient magnetic field changes. *Magn Reson Med* 2002;47:1052–1058.
7. Xiong J, Fox PT, Gao JH. Directly mapping magnetic field effects of neuronal activity by magnetic resonance imaging. *Hum Brain Mapp* 2003;20:41–49.
8. Mansfield P. Multi-planar image formation using NMR spin echos. *J Physics* 1977;C10:L55–L58.
9. Blum MJ, Braun M, Rosenfeld D. Fast magnetic resonance imaging using spiral trajectories. *Australas Phys Eng Sci Med* 1987;10:79–87.
10. McGibney G, Smith MR, Nichols ST, Crawley A. Quantitative evaluation of several partial Fourier reconstruction algorithms used in MRI. *Magn Reson Med* 1993;30:51–59.
11. Tsao J, Behnia B, Webb AG. Unifying linear prior-information-driven methods for accelerated image acquisition. *Magn Reson Med* 2001;46: 652–660.
12. van Vaals JJ, Brummer ME, Dixon WT, Tuithof HH, Engels H, Nelson RC, Gerety BM, Chezmar JL, den Boer JA. “Keyhole” method for accelerating imaging of contrast agent uptake. *J Magn Reson Imaging* 1993; 3:671–675.

13. Zientara GP, Panych LP, Jolesz FA. Dynamically adaptive MRI with encoding by singular value decomposition. *Magn Reson Med* 1994;32: 268–274.
14. Weaver JB, Xu Y, Healy DM, Driscoll JR. Wavelet-encoded MR imaging. *Magn Reson Med* 1992;24:275–287.
15. Ogawa S, Lee TM, Stepnoski R, Chen W, Zhu XH, Ugurbil K. An approach to probe some neural systems interaction by functional MRI at a neural time scale down to milliseconds. *Proc Natl Acad Sci USA* 2000;97:11026–11031.
16. Sodickson DK, Manning WJ. Simultaneous acquisition of spatial harmonics (SMASH): fast imaging with radiofrequency coil arrays. *Magn Reson Med* 1997;38:591–603.
17. Griswold MA, Jakob PM, Heidemann RM, Nittka M, Jellus V, Wang J, Kiefer B, Haase A. Generalized autocalibrating partially parallel acquisitions (GRAPPA). *Magn Reson Med* 2002;47:1202–1210.
18. Pruessmann KP, Weiger M, Scheidegger MB, Boesiger P. SENSE: sensitivity encoding for fast MRI. *Magn Reson Med* 1999;42:952–962.
19. Sodickson DK, McKenzie CA. A generalized approach to parallel magnetic resonance imaging. *Med Phys* 2001;28:1629–1643.
20. Lin FH, Huang TY, Chen NK, Wang FN, Stufflebeam SM, Belliveau JW, Wald LL, Kwong KK. Functional MRI using regularized parallel imaging acquisition. *Magn Reson Med* 2005;54:343–353.
21. de Zwart JA, Ledden PJ, Kellman P, van Gelderen P, Duyn JH. Design of a SENSE-optimized high-sensitivity MRI receive coil for brain imaging. *Magn Reson Med* 2002;47:1218–1227.
22. de Zwart JA, Ledden PJ, van Gelderen P, Bodurka J, Chu R, Duyn JH. Signal-to-noise ratio and parallel imaging performance of a 16-channel receive-only brain coil array at 3.0 Tesla. *Magn Reson Med* 2004;51: 22–26.
23. Wiggins GC, Potthast A, Triantafyllou C, Lin F-H, Benner T, Wiggins CJ, Wald LL. A 96-channel MRI system with 23- and 90-channel phase array head coils at 1.5 Tesla. In: Proceedings of the 13th Annual Meeting of ISMRM, Miami Beach, FL, USA, 2005. p 671.
24. Wiggins GC, Triantafyllou C, Potthast A, Reykowski A, Nittka M, Wald LL. A 32 channel receive-only phased array head coil for 3T with novel geodesic tiling geometry. In: Proceedings of the 13th Annual Meeting of ISMRM, Miami Beach, FL, USA, 2005. p 671.
25. Hamalainen M, Hari R, Ilmoniemi R, Knuutila J, Lounasmaa O. Magnetoencephalography-theory, instrumentation, and application to non-invasive studies of the working human brain. *Rev Mod Physics* 1993; 65:413–497.
26. Haacke EM. Magnetic resonance imaging: physical principles and sequence design. New York: J. Wiley & Sons; 1999. xxvii, 914 p.
27. McDougall MP, Wright SM. 64-channel array coil for single echo acquisition magnetic resonance imaging. *Magn Reson Med* 2005;54:386–392.
28. Willig-Onwuachi JD, Yeh EN, Grant AK, Ohliger MA, McKenzie CA, Sodickson DK. Phase-constrained parallel MR image reconstruction. *J Magn Reson* 2005;176:187–198.
29. Bydder M, Robson MD. Partial Fourier partially parallel imaging. *Magn Reson Med* 2005;53:1393–1401.
30. Lin FH, Kwong KK, Belliveau JW, Wald LL. Parallel imaging reconstruction using automatic regularization. *Magn Reson Med* 2004;51: 559–567.
31. Hansen PC. Rank-deficient and discrete ill-posed problems: numerical aspects of linear inversion. Philadelphia: SIAM; 1998. xvi, 247 p.
32. Lin FH, Belliveau JW, Dale AM, Hamalainen MS. Distributed current estimates using cortical orientation constraints. *Hum Brain Mapp* 2005; 27:1–13.
33. Sodickson DK. Tailored SMASH image reconstructions for robust in vivo parallel MR imaging. *Magn Reson Med* 2000;44:243–251.
34. Liu AK, Belliveau JW, Dale AM. Spatiotemporal imaging of human brain activity using functional MRI constrained magnetoencephalography data: Monte Carlo simulations. *Proc Natl Acad Sci USA* 1998;95: 8945–8950.
35. Liu AK, Dale AM, Belliveau JW. Monte Carlo simulation studies of EEG and MEG localization accuracy. *Hum Brain Mapp* 2002;16:47–62.
36. Dale AM, Liu AK, Fischl BR, Buckner RL, Belliveau JW, Lewine JD, Halgren E. Dynamic statistical parametric mapping: combining fMRI and MEG for high-resolution imaging of cortical activity. *Neuron* 2000; 26:55–67.
37. Worsley KJ, Liao CH, Aston J, Petre V, Duncan GH, Morales F, Evans AC. A general statistical analysis for fMRI data. *Neuroimage* 2002;15: 1–15.
38. Lin F-H, Kwong KK, Chen Y-J, Belliveau JW, Wald LL. Reconstruction of sensitivity encoded images using regularization and discrete time wavelet transform estimates of the coil maps. In: Proceedings of the 10th Annual Meeting of ISMRM, Honolulu, HI, USA, 2002. p 2389.
39. Friston KJ, Holmes AP, Poline JB, Grasby PJ, Williams SC, Frackowiak RS, Turner R. Analysis of fMRI time-series revisited. *Neuroimage* 1995; 2:45–53.
40. Liu G, Sobering G, Duyn J, Moonen CT. A functional MRI technique combining principles of echo-shifting with a train of observations (PRESTO). *Magn Reson Med* 1993;30:764–768.
41. Lin FH, Witzel T, Ahlfors SP, Stufflebeam SM, Belliveau JW, Hamalainen MS. Impact of regularization on the point-spread function of the MEG minimum-norm estimates. In: Proceedings of the 14th International Conference on Biomagnetism, Boston, MA, USA, 2004. p 485.
42. Tsao J, Boesiger P, Pruessmann KP. k-t BLAST and k-t SENSE: dynamic MRI with high frame rate exploiting spatiotemporal correlations. *Magn Reson Med* 2003;50:1031–1042.
43. Golub GH, Heath MT, Wahba G. Generalized cross-validation as a method for choosing a good ridge parameter. *Technometrics* 1979;21: 215–223.
44. Kruger G, Glover GH. Physiological noise in oxygenation-sensitive magnetic resonance imaging. *Magn Reson Med* 2001;46:631–637.